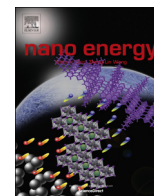




ELSEVIER

Contents lists available at ScienceDirect

Nano Energy

journal homepage: www.elsevier.com/locate/nanoen

Carbon-based electrocatalyst derived from bimetallic metal-organic framework arrays for high performance oxygen reduction



Zhenhua Li, Mingfei Shao*, Lei Zhou, Qihui Yang, Cong Zhang, Min Wei*, David G. Evans, Xue Duan

State Key Laboratory of Chemical Resource Engineering, Beijing University of Chemical Technology, Beijing 100029, China

ARTICLE INFO

Article history:

Received 15 March 2016

Received in revised form

20 April 2016

Accepted 21 April 2016

Available online 22 April 2016

Keywords:

Carbon-based networks

Bimetallic metal-organic frameworks

Layered double hydroxides

Oxygen reduction reaction

ABSTRACT

Electrocatalysts for oxygen reduction reaction (ORR) play a key role in renewable energy technologies including metal-air batteries and fuel cells. Despite tremendous efforts, the development of ORR electrocatalysts with high activity and low cost remains a great challenge. Here, we report the fabrication of well-defined carbon network with honeycomb-like structure as a high-performance catalyst toward ORR, *via* pyrolysis of bimetallic Co, Zn-zeolitic imidazolate (Co, Zn-ZIF) crystal arrays grown on the surface of layered double hydroxide nanoplatelets (LDHs@Co, Zn-ZIF). The concentration of doped-heteroatoms (N, Co), the graphitic degree as well as the surface porosity of the resulting carbon network can be finely controlled by tuning the Co/Zn molar ratio in the LDHs@Co, Zn-ZIF precursors. The optimal carbon catalyst (CoZn-2) exhibits excellent ORR activity with an onset potential of 0.976 V vs. RHE and a limited current density of 5.8 mA cm^{-2} , which is superior to commercial Pt/C catalyst. In addition, both an extraordinary long-term stability ($\sim 99.5\%$ current retention over 20,000 s) and a strong tolerance against methanol corrosion are also obtained. This work demonstrates an effective strategy to artificially regulate the nanostructure and intrinsic active site of carbon-based ORR electrocatalysts.

© 2016 Elsevier Ltd. All rights reserved.

1. Introduction

The design of highly active and cost-effective catalysts for energy storage and conversion applications is a critical strategy in the pursuit of sustainable energy [1–3]. The oxygen reduction reaction (ORR) in particular is an enabling process for many energy storage options, such as fuel cells and metal-air batteries [4–6]. So far, Pt based materials have been the dominant and efficient electrocatalysts toward ORR [7–9], but the scarcity, high cost and low stability of Pt largely limit its practical applications. In this regard, a broad range of alternative catalysts have been actively pursued including nonprecious metals (Fe, Co, etc.) [10,11], metallic compounds (e.g., oxides, chalcogenides, nitrides and oxynitrides) [12–15] as well as heteroatoms-doped carbon materials [16–18]. However, for a given catalyst, high activity and long-time durability are practically hard to be achieved simultaneously as a consequence of some intrinsic limitations of individual constitution. To promote the performance of ORR catalysts, many efforts have been developed by tuning the intrinsic active site for catalytic reactions or constructing nanostructures to enhance mass

transport and facilitate the active site exposure [19,20]. In spite of all these progresses, how to achieve satisfactory ORR catalysts by virtue of material exploration and fabrication strategy is still a huge challenge.

Recently, heteroatoms-doped carbon materials have been emerging as promising and cost-effective alternatives for promoting the ORR [21–23]. Aiming to discover highly active carbon-based materials, high graphitized carbon, uniformly doped heteroatoms (especially N, for the formation of C–N bonding as active site) as well as porous nanostructure are widely explored as ORR activity descriptors [24–26]. However, the well-graphitized carbon with efficient dopants (e.g., N and Co) is practically hard to be satisfied due to the more favorable formation of C–C bond than C–N or C–Co bond in a pyrolysis process [27,28]. Moreover, the pyrolysis process usually leads to a serious fusion and aggregation of carbon nanoparticles, giving rise to a limited active site exposure and blocking the tunnels of mass transfer [29,30]. Consequently, it is urgent to precisely optimize the active sites and porous structures simultaneously over carbon-based catalysts for better guiding the design of advanced ORR catalysts.

In our previous work, carbon-based network has been prepared *via* directed growth of metal-organic framework (MOF) crystal arrays on the surface of layered double hydroxides (LDHs) followed by a pyrolysis treatment, which shows good ORR properties [31]. Although the introduction of LDHs as a directing agent

* Corresponding authors.

E-mail addresses: shaomf@mail.buct.edu.cn (M. Shao), weimin@mail.buct.edu.cn (M. Wei).

guarantees the formation of well-organized carbon, a precise control over the active sites (i.e., the doped heteroatoms: Co, N) and the porous network is not achieved yet. Herein, we further fabricate a well-defined two dimensional (2D) carbon-based architecture with simultaneously fine control over active sites and porosity by pyrolysis of bimetallic Co, Zn-zeolitic imidazolate (Co, Zn-ZIF) framework grown on the surface of LDHs nanoplatelets, which exhibits significantly enhanced electrocatalytic ORR performances. It is found that the Co species in the Co, Zn-ZIF precursor provides highly graphitized carbon with good conductivity; while the Zn element is helpful to form high-surface-area carbon with N-doping. By tuning the Co/Zn molar ratio, the optimal carbon network gives a decisive contribution to the excellent ORR activity (with an onset potential of 0.976 V vs. RHE and ~99.5% current retention over 20,000 s), which is superior to the commercial Pt/C catalyst and among the best in all of the MOF-derived ORR catalysts reported to date.

2. Experimental section

2.1. Preparation of CoAl-LDH template

The sample of CoAl-LDH with well-defined hexagonal morphology was prepared in a three-neck flask equipped with a reflux condenser under a nitrogen flow. Typically, $\text{CoCl}_2 \cdot 6\text{H}_2\text{O}$ (10 mM), $\text{AlCl}_3 \cdot 6\text{H}_2\text{O}$ (5 mM) and urea (35 mM) were dissolved in 400 mL of deionized water. The solution was then heated at 97 °C under refluxing with continuous stirring for 48 h. The resulting product was filtered, washed with deionized water and ethanol for several times, and finally dried at ambient temperature in air.

2.2. Preparation of LDHs@Co,Zn-ZIF precursors

As a typical representative, the synthesis of LDHs@Co, Zn-ZIF with a Co/Zn molar ratio of 2 was performed as follows: a 100 mL of methanol solution containing CoAl-LDH (0.1 g), $\text{Co}(\text{NO}_3)_2 \cdot 6\text{H}_2\text{O}$ (0.1 M) and $\text{Zn}(\text{NO}_3)_2 \cdot 6\text{H}_2\text{O}$ (0.05 M) was firstly prepared. Then a 2-methylimidazole (MeIm) methanol solution (50 mL, 0.8 M) was rapidly poured into the above solution under magnetic stirring at room temperature for 15 min. The product was collected by centrifugation (3000 rpm, 5 min) and washed several times by methanol. Other LDHs@Co, Zn-ZIF precursors with different Co/Zn molar ratios were obtained by changing the concentration of $\text{Zn}(\text{NO}_3)_2 \cdot 6\text{H}_2\text{O}$ to 0.4 M (Co/Zn=0.25), 0.2 M (Co/Zn=0.5), 0.1 M (Co/Zn=1), 0.033 M (Co/Zn=3) and 0.025 M (Co/Zn=4), respectively. The resulting LDHs@Co, Zn-ZIF precursors in this stage are denoted as LDH@ZIF-CoZn- x ($x=0.25, 0.5, 1, 2, 3$ and 4).

2.3. Preparation of carbon-based ORR electrocatalysts

The as-prepared LDHs@Co, Zn-ZIF precursors were placed in a ceramic boat and transferred into a temperature-programmed furnace. The pyrolysis treatment was performed at 600–800 °C for 2 h with a heating rate of 5 °C min^{-1} in N_2 atmosphere; the final pyrolysis products are denoted as CoZn- x ($x=0.25, 0.5, 1, 2, 3, 4$).

2.4. Characterizations

X-ray diffraction patterns were collected on a Shimadzu XRD-6000 diffractometer using a Cu $K\alpha$ source, with a scan step of 0.02° and a scan range between 3° and 70°. FTIR spectra were recorded on a NICOLET NEXUS470 Fourier transform infrared spectrometer. X-ray photoelectron spectra (XPS) were performed on a Thermo VG ESCALAB 250 X-ray photoelectron spectrometer at a pressure of about 2×10^{-9} Pa using Al $K\alpha$ X-rays as the excitation source.

Raman measurements were carried out with 532 nm of excitation by using a confocal Raman microspectrometer (Renishaw, inVia-Reflex, 532 nm). The specific surface area determination, pore size analysis were performed by Brunauer–Emmett–Teller (BET) and Barrett–Joyner–Halenda (BJH) method, respectively, using a Quantachrome Autosorb-1CVP analyzer. Prior to the measurements, the samples were degassed at 150 °C for 8 h. The morphology was investigated using a scanning electron microscope (SEM; Zeiss SUPRA 55) with an accelerating voltage of 20 kV, combined with energy dispersive X-ray spectroscopy (EDX) for the determination of carbon-based materials. Transmission electron microscope (TEM) images were recorded using a Philips Tecnai 20 and JEOL JEM-2010 high-resolution transmission electron microscopes with an accelerating voltage of 200 kV in each case. A Tecnai G2 F30 S-TWIN microscope operated at 300 kV was employed to reveal the honeycomb-like structure using the scanning transmission electron microscope (STEM).

2.5. Electrochemical measurements

All the electrochemical experiments were performed by using a CHI660E electrochemical workstation (Shanghai Chenhua Instrument Co., China) at room temperature in 0.1 M KOH solution or 0.1 M HClO_4 solution with a conventional three-electrode cell. The reference electrode is a saturated Ag/AgCl electrode in 0.1 M KOH solution or a saturated calomel electrode (SCE) in 0.1 M HClO_4 solution. The counter electrode is a platinum wire. A rotating disk electrode (RDE) of 3.0 mm in diameter and rotating ring-disk electrode (RRDE) of 5.61 mm in diameter were used as the substrate for the working electrode. Prior to use, RDE and RRDE were polished by aqueous alumina suspensions on felt polishing pads, and washed with deionized water and ethanol. To prepare the working electrode, the catalyst (2 mg) was dispersed in the solution containing 780 μL of deionized water, 200 μL of ethanol and 20 μL of 5 wt% Nafion solution, followed by a strong ultrasonic treatment to form a uniform black ink. 7 μL of the catalyst ink was dripped onto the glassy carbon surface with a loading of 0.2 mg cm^{-2} for all samples including commercial Pt/C catalyst (20 wt% of Pt). Before test, a N_2 or O_2 flow was used for the electrolyte in the cell for 30 min to give a saturation state. The cyclic voltammetry (CV) experiments were performed in N_2 - and O_2 -saturated 0.1 M KOH solution or 0.1 M HClO_4 solution at a scan rate of 10 mV s^{-1} . RDE tests were measured in O_2 -saturated 0.1 M KOH solution or 0.1 M HClO_4 solution at different speed rates (625, 900, 1225, 1600, 2025, 2500 rpm) with a sweep rate of 10 mV s^{-1} . RRDE measurements were also conducted in O_2 -saturated 0.1 M KOH solution or 0.1 M HClO_4 solution at room temperature. The disk potential was cycled from 0–1.1 V vs. RHE at a scan rate of 5 mV s^{-1} and the ring potential was set at 1.3 V vs. RHE. The stability tests were carried out at 0.5 V vs. RHE in O_2 -saturated 0.1 M KOH ($\omega=1600$ rpm) by the chronoamperometric method. During the crossover tests, 2 M methanol was added into O_2 -saturated 0.1 M KOH within ~200 s.

The Koutecky–Levich equation was used to calculate the kinetics parameters:

$$\frac{1}{j} = \frac{1}{j_L} + \frac{1}{j_k} = \frac{1}{B\omega^{1/2}} + \frac{1}{j_k}$$

$$B = 0.62nFC_0(D_0)^{2/3}\nu^{-1/6}$$

$$j_k = nFkC_0$$

where j is the measured current density; j_k and j_L are the kinetic-

and diffusion-limiting current density; ω is the electrode rotating rate; F is the Faraday constant ($F=96,485 \text{ C mol}^{-1}$); C_0 is the bulk concentration of O_2 ($1.20 \times 10^{-6} \text{ mol cm}^{-3}$ for both 0.1 M KOH and 0.1 M HClO_4 solution); D_0 is the diffusion coefficient of O_2 ($1.90 \times 10^{-5} \text{ cm}^2 \text{ s}^{-1}$ for 0.1 M KOH solution and $1.93 \times 10^{-5} \text{ cm}^2 \text{ s}^{-1}$ for 0.1 M HClO_4 solution); ν is the kinematic viscosity of the electrolyte ($0.01 \text{ cm}^2 \text{ s}^{-1}$ for both 0.1 M KOH and 0.1 M HClO_4 solution), and k is the electron transfer rate constant.

The electron transfer number and the peroxide percentage can be calculated by the following equations:

$$n = 4 \times \frac{i_d}{i_r/N + i_d}$$

$$\% \text{HO}_2^- = 200 \times \frac{i_r/N}{i_r/N + i_d}$$

where i_d is the disk current; i_r is the ring current and N is the current collection efficiency of the Pt ring ($N=0.37$).

ECSA values of $\text{CoZn-}x$ samples and Pt/C catalyst were determined by measuring the capacitive current associated with double-layer charging from the scan-rate dependence of CVs. The ECSA was measured on the same working electrode and electrolyte (0.1 M KOH). The potential window of CVs was 1–1.1 V vs. RHE, and the scan rates were 20, 40, 60, 80 and 100 mV/s. The double layer capacitance (C_{dl}) was estimated by plotting the Δj ($j_a - j_c$) at 1.05 V vs. RHE against the scan rate. The slope is twice of C_{dl} .

For the Tafel plot, the kinetic current was calculated from the mass-transport correction of RDE by

$$J_K = \frac{J \times J_L}{J - J_L}$$

The measured potential vs. the reference electrode was converted to the reversible hydrogen electrode (RHE) scale via the Nernst equation:

$$E_{RHE} = E_{Ref} + 0.059pH + E_{Ref}^0$$

where E_{RHE} is the converted potential vs. RHE; E_{Ref} is the experimental potential measured against the reference electrode, and E_{Ref}^0 is the standard potential of the reference electrode at 25 °C.

For the electrochemical measurements carried out in 0.1 M KOH, the conversion from Ag/AgCl to RHE is

$$E_{RHE} = E_{Ag/AgCl} + 0.964 \text{ V}$$

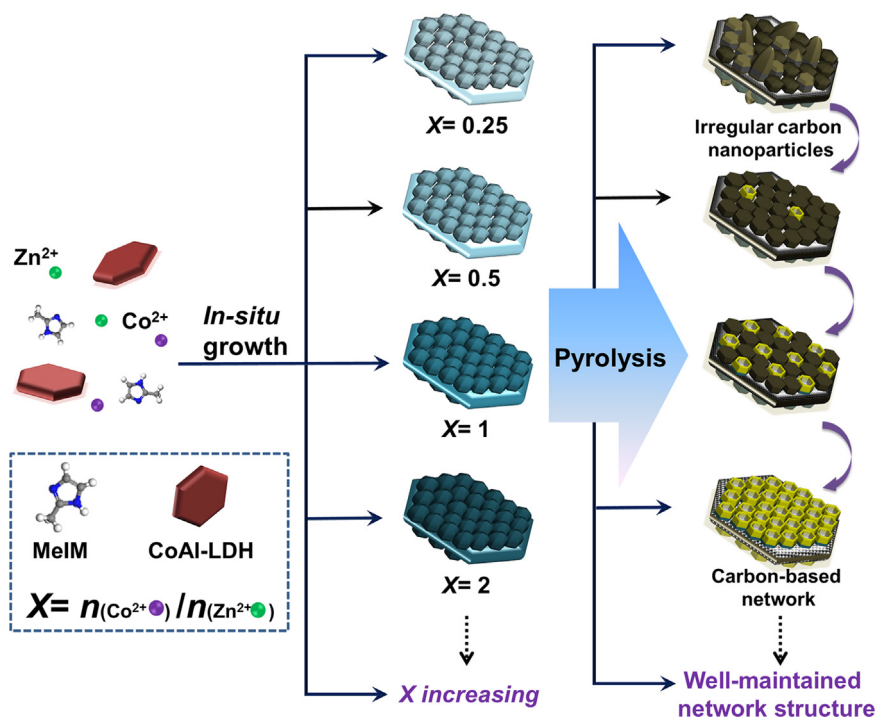
As for SCE in 0.1 M HClO_4 solution, the conversion from SCE to RHE is

$$E_{RHE} = E_{SCE} + 0.304 \text{ V}$$

3. Results and discussion

3.1. Materials preparation and characterization

The carbon-based architecture is fabricated via a two-step procedure (Scheme 1): *in situ* growth of Co, Zn-ZIF crystal arrays on the surface of CoAl-LDH nanoplatelets, followed by a subsequent pyrolysis treatment. Firstly, CoAl-LDH nanoplatelet with well-defined hexagonal morphology ($\sim 6 \mu\text{m}$ in lateral size; Fig. S1) was synthesized via a hydrothermal method. Then, the LDH supported Co, Zn-ZIF crystal arrays with various Co/Zn molar ratios were prepared by an *in situ* growth method at room temperature. The obtained precursors in this stage with sandwich-like structure are denoted as LDH@ZIF-CoZn- x (x is the molar ratio of $\text{Co}^{2+}/\text{Zn}^{2+}$ in Co, Zn-ZIF; $x=0.25, 0.5, 1, 2, 3$ and 4, respectively), in which Co, Zn-ZIF crystals uniformly grow on both sides of CoAl-LDH nanoplatelet (Figs. S2 and S3). The molar ratios of Co/Zn are determined by the X-ray spectroscopy (EDX), which is close to the feed ratios (Fig. S4 and Table S1). Then, the LDH@ZIF-CoZn- x were pyrolyzed in a temperature-programmed furnace with nitrogen gas flow at 800 °C for 2 h and the final products are denoted as CoZn- x . SEM image (Fig. 1(a)) shows some irregular carbon nanoparticles stacking on the surface of the pyrolysis product for CoZn-0.25. With the increase of Co/Zn molar ratio from 0.25 to 1,



Scheme 1. A schematic illustration for the synthesis of LDH@ZIF-CoZn- x precursors and the resulting carbon-based architectures.

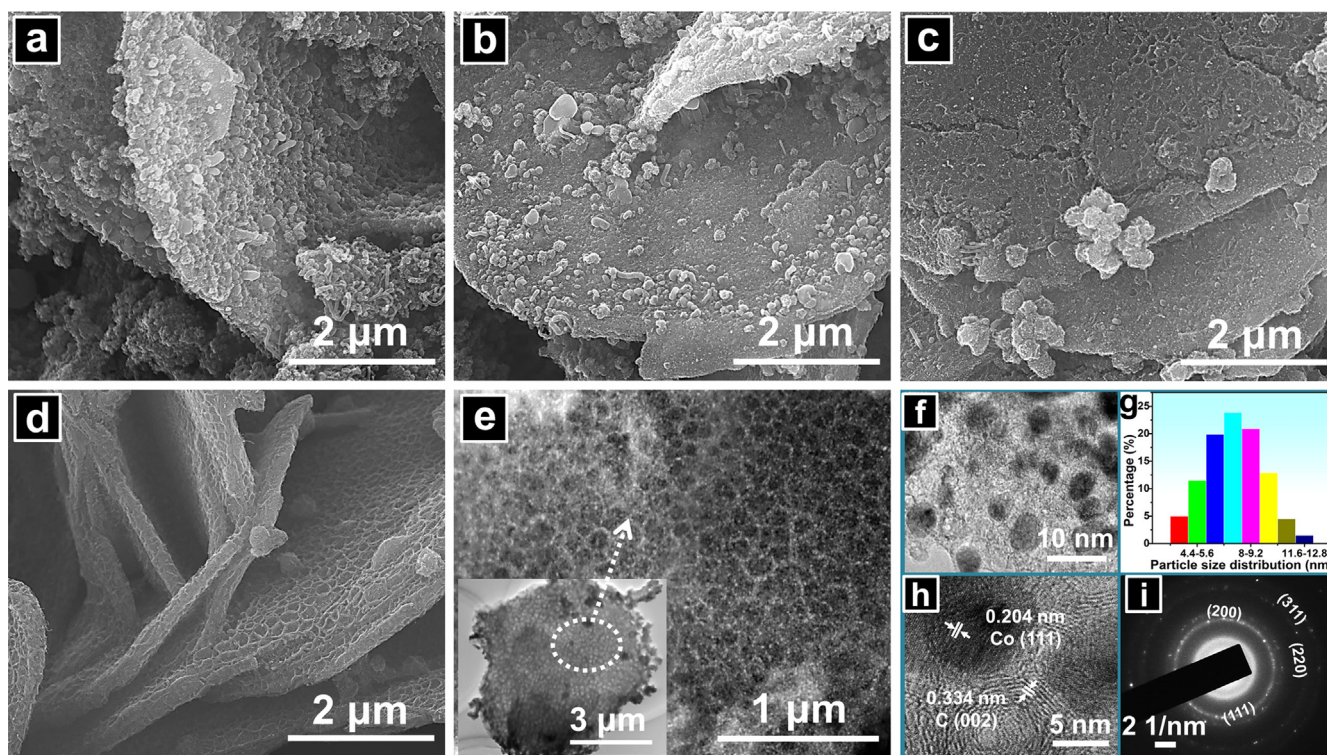


Fig. 1. SEM images of (a) CoZn-0.25, (b) CoZn-0.5, (c) CoZn-1 and (d) CoZn-2. (e) STEM images of CoZn-2. (f) HRTEM image of CoZn-2 and (g) corresponding particle size distribution of Co nanoparticles. (h) Magnified HRTEM image of CoZn-2 and (i) corresponding SAED pattern.

the carbon nanoparticles in the pyrolysis product disappear at first (Fig. 1(b), CoZn-0.5) and then honeycomb-like nanostructure is observed on the surface of nanoplatelet (Fig. 1(c), CoZn-1). As x increases to 2, a typical 2D porous structure comes into formation with continuous honeycomb-like carbon framework (Fig. 1(d), CoZn-2); this structure can be well maintained with further increase of x to 4 (Fig. S5a for CoZn-3 and Fig. S5b for CoZn-4). This verifies that the cobalt species in Co, Zn-ZIF crystal arrays is helpful for the formation of 2D ordered carbon architecture.

STEM images of CoZn-2 reveals a 2D porous morphology with a lateral particle size of $\sim 6 \mu\text{m}$, close to the size of CoAl-LDH template (Fig. 1(e), inset). The obtained honeycomb holes are $\sim 200 \text{ nm}$ in diameter, also corresponding to the original ZIF crystals. The more detailed nanostructure of CoZn-2 was investigated by HRTEM. As shown in Fig. 1(f), well-dispersed nanoparticles with a narrow particle size centered at $\sim 7 \text{ nm}$ in diameter are observed (Fig. 1(g)). Around the nanoparticles, graphite-like layers can be easily identified with an interlayer spacing of 0.334 nm , corresponding to the (002) plane of graphitic carbon (Fig. 1(h)) [32]. The HRTEM image combined with SAED pattern further demonstrates the existence of metallic Co nanoparticles with well-resolved (111) lattice fringe of 0.204 nm (Fig. 1(h) and (i)) [33]. The detailed nanostructure and graphitic degree for other carbon products were also demonstrated by HRTEM. As shown in Fig. S6, the carbon-based network derived from LDH@ZIF-CoZn-0.5 gives a smaller Co nanoparticles ($1\text{--}2 \text{ nm}$ in diameter) surrounded by amorphous carbon, indicating that a lower Co content inhibits the formation of well-graphitized carbon.

Fig. 2(a) shows the XRD patterns of LDH@ZIF-CoZn- x derived carbon-based materials. All these samples display clear (111) and (200) crystal planes of face-centered-cubic (fcc) Co diffraction at 2θ 44° and 51° [34], and the intensities of the two peaks enhances gradually with the increase of Co content in the LDHs@Co, Zn-ZIF precursors (Co/Zn molar ratio: from 0.25 to 4). However, no diffraction related to Zn is found in all these samples, owing to the facile

evaporation of Zn in the pyrolysis process [35]. This is also proved by the EDX spectra (Fig. S7 and Table S2) and the full XPS spectra (Fig. S8 and Table S3), in which signals of C, N, O and Co element are observed while only trace Zn is detected in the pyrolysis products. The chemical compositions and surface properties for CoZn- x materials are further studied. Based on the Raman spectra (Fig. S9), the intensity ratio of G band to D band (I_G/I_D) for CoZn- x increases from 0.69 to 0.97 along with the enhancement of x from 0.25 to 4 (Fig. 2(b)), indicating a gradually increased graphitization degree [36]. In contrast, the content of N gives an inverse trend: CoZn-0.25 (8.66 at%) > CoZn-0.5 (8.49 at%) > CoZn-1 (7.58 at%) > CoZn-2 (6.94 at%) > CoZn-3 (6.35 at%) > CoZn-4 (5.58 at%). The result shows that Co element in the Co, Zn-ZIF precursors facilitate the formation of graphitic carbons; while Zn is helpful to improve the N-doping in the obtained carbon nanostructure.

The surface area and pore-size distribution of CoZn- x are investigated by N_2 -adsorption/desorption measurements. Typical IV-type isotherms with sharp uptakes at low relative pressure (< 0.05) and H3-type hysteresis loops (uptakes at a relative pressure ranging from 0.45 to 1.0) are observed for all the pyrolysis samples (Fig. S10), indicating the coexistence of micropore and mesopore [37]. According to the Barrett–Joyner–Halenda (BJH) model, Fig. 2(c) shows that all these CoZn- x materials have a relatively broad pore diameter with a maximum frequency at ~ 2 and 85 nm , respectively. In addition, a new pore size (centered at $\sim 12 \text{ nm}$) appears along with the formation of honeycomb-like structure (Fig. 2(c)). The specific surface area (S_{BET}) of CoZn- x materials, which is determined by the Brunauer–Emmett–Teller (BET) method (Fig. 2(d)), increases significantly from $185 \text{ m}^2 \text{ g}^{-1}$ (CoZn-0.25) to $429 \text{ m}^2 \text{ g}^{-1}$ (CoZn-2), but decreases to $385 \text{ m}^2 \text{ g}^{-1}$ (CoZn-3) and $306 \text{ m}^2 \text{ g}^{-1}$ (CoZn-4). This result demonstrates that a suitable Co/Zn molar ratio can effectively improve the specific surface area and pore distribution of pyrolyzed carbon-based materials; while an excess of Co/Zn molar ratio leads to a decrease of S_{BET} , which may result from a dense packing of graphitized

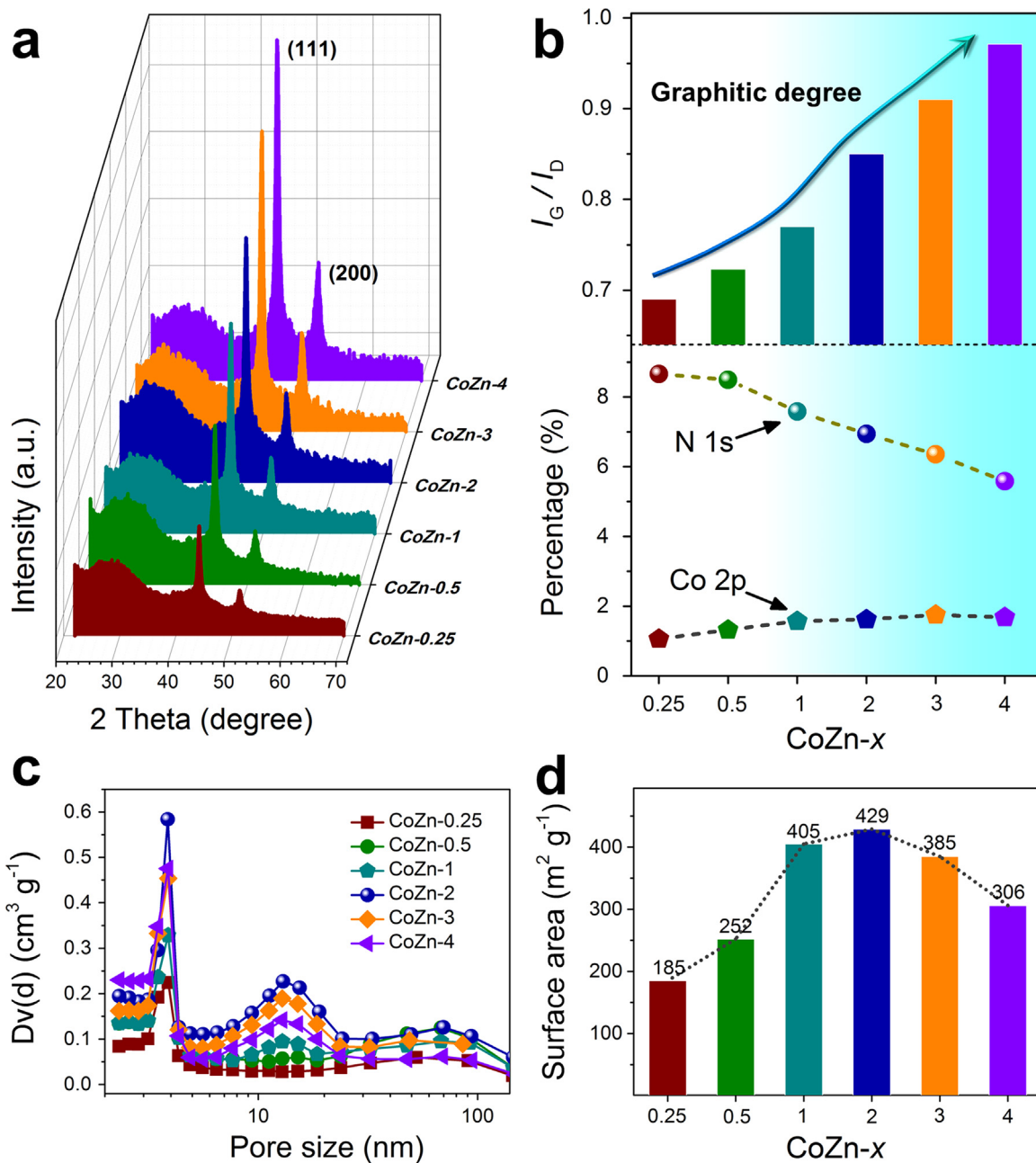


Fig. 2. (a) XRD patterns for CoZn-*x* materials. (b) The change of I_G/I_D values for CoZn-*x* based on the Raman spectra and the percentage of N and Co obtained from XPS spectra. (c) Pore-size distribution and (d) specific surface area of CoZn-*x* determined by N_2 -adsorption/desorption measurements.

carbon nanoparticles. It is believed that a unique hierarchical porous structure with enhanced mass transport and active site exposure can accelerate the catalytic reaction process [38], which will be discussed in the next section.

3.2. Enhanced ORR performance

We found that the pyrolysis temperature of 800 °C is the optimum parameter for obtaining the maximum ORR catalytic performance for CoZn-*x* (Figs. S11–S13). The cyclic voltammetry (CV) curves for all these CoZn-*x* materials exhibit a more obvious and well-defined cathodic peak in O_2 -saturated electrolyte than that in N_2 -saturated solution, indicating their electrocatalytic activities for ORR (Fig. S14). Among them, CoZn-2 shows the most positive reduction peak, predicting its superior ORR activity. Fig. 3(a) displays the linear sweep voltammetry (LSV) curves of these CoZn-*x*

materials, in which a typical oxygen reduction process with a sharply increased current at the mixed kinetic- and diffusion-controlled zone and an obvious platform at the diffusion-controlled zone are observed. Remarkably, CoZn-2 presents the highest diffusion-limited current density (5.8 mA cm^{-2}) among these catalysts derived from LDH@ZIF-CoZn-*x* (Figs. 3(a), S15 and S16); it also possesses the most positive onset potential (0.976 V vs. RHE) and half-wave potential (0.849 V vs. RHE; Fig. 3(b)), much higher than that of commercial Pt/C catalyst (Fig. S17; Table S4). In addition, the ORR performance of CoZn-2 is also significantly superior to that of pure CoAl-LDH template, LDH@MOF precursor (LDH@ZIF-CoZn-2) as well as CoAl-LDH calcinated at 800 °C in N_2 atmosphere (denoted as CoAl-LDH-800) (Fig. S18). It is worth mentioning that this performance of CoZn-2 is among the best in all of the reported MOF-derived ORR catalysts and other noble-metal free materials reported to date (see Table S5 for comparison).

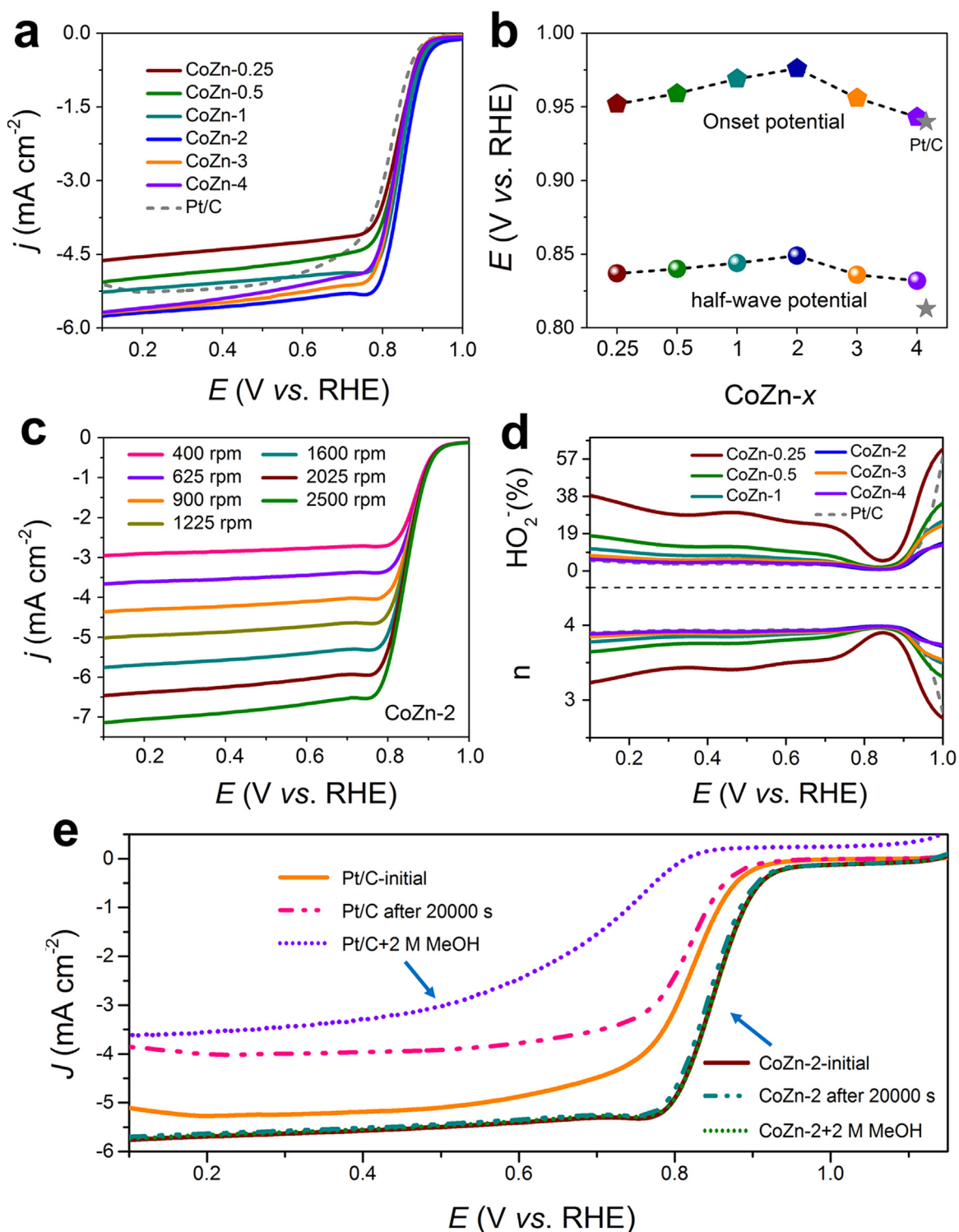


Fig. 3. (a) LSV curves for CoZn- x ($x=0.25, 0.5, 1, 2, 3, 4$) and Pt/C catalyst in O₂-saturated 0.1 M KOH solution with a sweep rate of 10 mV s⁻¹ and electrode rotation speed of 1600 rpm. (b) Corresponding onset potential and half-wave potential for CoZn- x and Pt/C. (c) LSV curves for CoZn-2 at various rotation rates. (d) Peroxide yield and electron transfer number of CoZn- x and Pt/C catalyst at various potentials based on the RRDE data. (e) LSV curves of CoZn-2 and commercial Pt/C before and after 20,000 s CA-measurements in O₂-saturated 0.1 M KOH solution at 1600 rpm, and the LSV curves of CoZn-2 and commercial Pt/C in O₂-saturated 0.1 M KOH solution with and without 2 M methanol.

The ORR electron-transfer process of CoZn- x is studied by RDE experiments at various rotating speeds at a scan rate of 10 mV s⁻¹ under O₂-saturated system (Fig. 3(c)), and the Koutecky–Levich (K–L) equation is used to analyze the kinetic parameters. As shown in Fig. S19 and Table S6, CoZn- x catalysts derived from the LDH@ZIF-CoZn- x precursors with a high Zn content ($x=0.25$ and

0.5) show a mixed two or four electron oxygen reduction process. The calculated results reveal an electron transfer number of ~ 2.76 for CoZn-0.25 and ~ 3.25 for CoZn-0.5 (0.2–0.7 V vs. RHE), mostly owing to the poor activity of catalysts with low graphitization degree. With the increase of Co/Zn molar ratio, the electron transfer number is elevated and a more immediate four electron

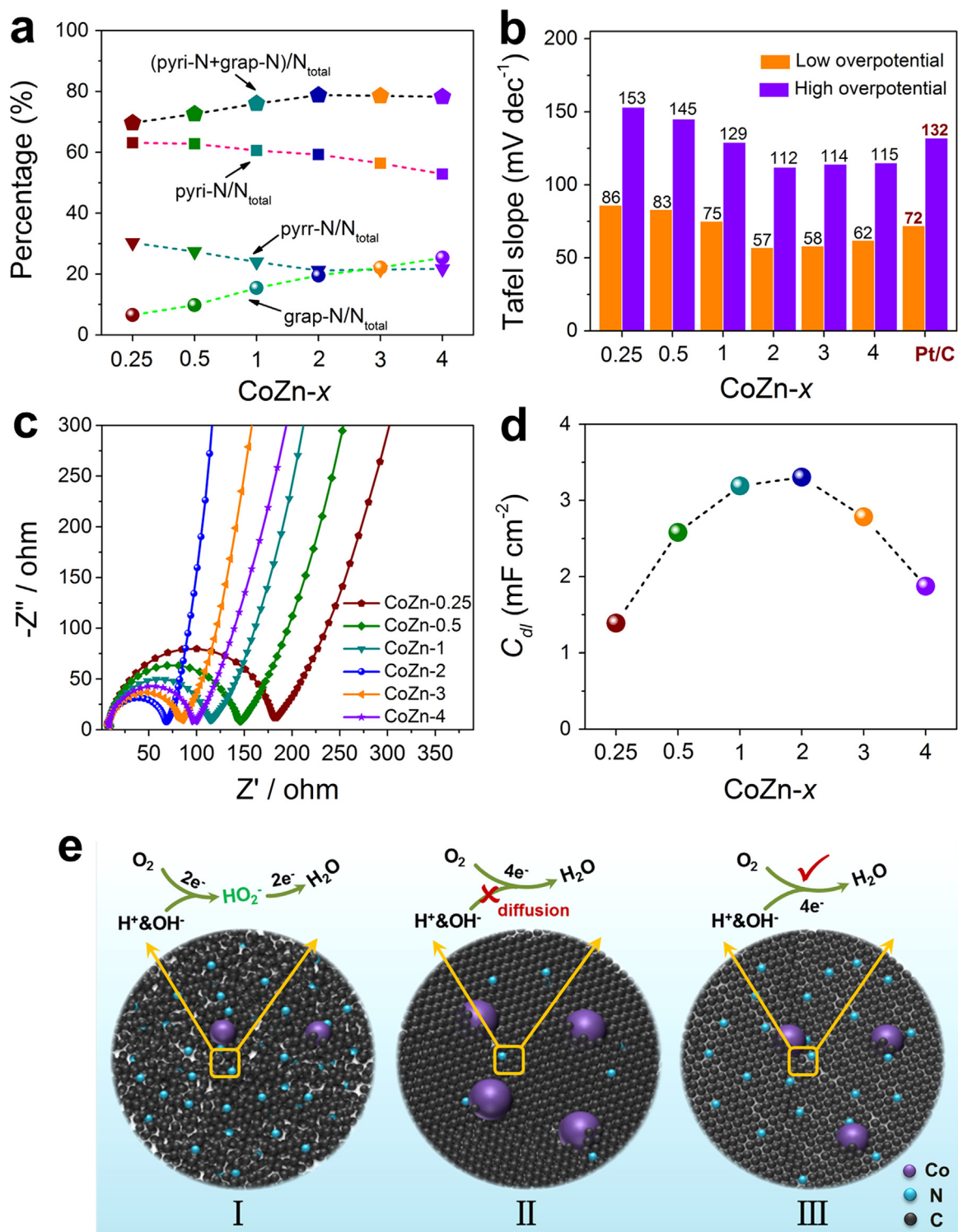


Fig. 4. (a) Percentage of various nitrogen species for CoZn-x obtained from XPS spectra. (b) Tafel slope values in low and high overpotential regions for CoZn-x and Pt/C catalyst. (c) EIS spectra of CoZn-x. (d) The double layer capacitance C_{dl} of CoZn-x, which is used to represent the ECSA. (e) Schematic illustration of the ORR process catalyzed by CoZn-x materials with different Co/Zn molar ratios and nanostructures (I: an excess Zn content; II: an excess Co content; III: an optimal Co/Zn molar ratio).

oxygen reduction process is demonstrated for CoZn-1 (~3.89), CoZn-2 (~3.96), CoZn-3 (~3.93) and CoZn-4 (~3.92), respectively. Furthermore, rotation ring-disk electrode (RRDE) was used to monitor the formation of HO_2^- during the ORR process (Fig. S20). As shown in Fig. 3(d), the HO_2^- yield is below 10% with the electron transfer number of 3.86–3.98 for CoZn-2, similar to that of Pt/C catalyst. However, the HO_2^- yield increases rapidly with the increase of Zn content in the LDHs@Co, Zn-ZIF precursors

(~35% for CoZn-0.5 and ~65% for CoZn-0.25), in accordance with the results obtained from the K-L plots based on the RDE measurements. This further demonstrates that an appropriate Co/Zn ratio in LDHs@Co, Zn-ZIF precursors can produce carbon materials with an optimum performance toward ORR.

The stability of the obtained carbon catalyst (CoZn-2) was evaluated by chronoamperometric (CA) and LSV measurements. As shown in Fig. 3(e), no obvious negative shift in the LSV curve of

CoZn-2 can be observed after 20,000 s of continuous CA operation, much superior to that of Pt/C catalyst (~ 31 mV negative shift in half-wave potential). CV curves show that the current density of CoZn-2 maintains $\sim 99.5\%$; while only 60% retention is found for the Pt/C catalyst (Fig. S21a). Moreover, with the addition of 2 M methanol, both the LSV curve (Fig. 3(c)) and CA curve (Fig. S21b) of CoZn-2 do not display variation; in contrast, Pt/C catalyst suffers a sharp loss in activity. This demonstrates that the CoZn-2 catalyst possesses a stronger tolerance against crossover effect than Pt/C catalyst. In addition, the CoZn-2 catalyst also shows a good ORR activity in acidic solution (0.1 M HClO₄). As shown in Fig. S22, the CoZn-2 catalyst exhibits an onset potential of 0.892 V vs. RHE, half-wave potential of 0.679 V vs. RHE and diffusion-limited current density of 5.3 mA cm⁻² at 0.2 V vs. RHE, much close to those of Pt/C catalyst. The HO₂⁻ yield of CoZn-2 in acidic solution is below 10% and the electron transfer number (*n*) ranges in 3.85–3.96, also close to Pt/C and consistent with the results obtained from the K–L plots based on the RDE study (Fig. S23).

3.3. Discussion

As demonstrated above, the ORR activity of the obtained carbon-based materials can be optimized by tuning the Co/Zn molar ratio in the Co, Zn-ZIF precursor. We make further discussion to reveal the intrinsic reason for this interesting result. As reported previously, the type of nitrogen species plays a crucial role in the N-doped carbon-based ORR catalysts [39]. We employed XPS to investigate the variation of N species in these CoZn-*x* materials (Fig. S24). The N 1s spectra of all the CoZn-*x* samples can be mainly deconvoluted into three peaks: pyridinic-N (pyri-N, 398.3 eV), pyrrolic-N (pyrr-N, 400.2 eV), and graphitic-N (grap-N, 401.2 eV). It has been reported that both the pyri-N and grap-N play a crucial role in the ORR process while the contribution of pyrr-N is uncertain [40]. The relative composition of the three types of N is shown in Fig. 4(a) and Table S7. With the increase of Co/Zn molar ratio, the relative composition of pyri-N reduces gradually, while that of grap-N increases significantly. The relative composition summation of pyri-N and grap-N shows an increase from 69.68% to 78.81% along with the enhancement of Co/Zn ratio from 0.25 to 2, followed by a slight decline for CoZn-3 (78.54%) and CoZn-4 (78.28%), which is due to the larger reduction rate of pyri-N than the growth rate of grap-N. This change is in agreement with the trend of ORR activity for CoZn-*x*, indicating pyri-N and grap-N act as active sites toward ORR.

To analyze the kinetic properties of ORR, the tafel slopes for CoZn-*x* and Pt/C catalyst were obtained from the linear plots of LSVs at 1600 rpm (Fig. S25). All of these plots show typical two-stage linear regions at low overpotential (η_L ; where the overall ORR speed is determined by the surface reaction rate) and high overpotential (η_H ; where the overall ORR rate is dependent on the oxygen diffusion) [41]. As shown in Fig. 4(b), both the tafel slopes at η_L (57 mV dec⁻¹) and η_H (112 mV dec⁻¹) for the CoZn-2 are much lower than those of CoZn-*x* (with other Co/Zn molar ratios) and commercial Pt/C catalyst, further proving that the CoZn-2 possesses a faster electron transfer rate and more efficient reactant diffusion toward ORR. This can be demonstrated by the results of electrochemical impedance spectroscopy (EIS) and electrochemical surface areas (ECSA) of these CoZn-*x* catalysts. The EIS measurements in the ORR region at 0.85 V vs. RHE are conducted [35] and the corresponding Nyquist plots of the EIS spectra are shown in Fig. 4(c). All of the curves for CoZn-*x* catalysts consist of a semicircle in high frequency region and a straight line in low frequency region. The semicircle diameter reflects the charge transfer resistance, and the slope of straight line indicates the ion diffusion resistance. The CoZn-2 shows a smaller semicircle diameter and a larger slope, which indicates a faster electron

transport kinetics and ion diffusion rate [42,43]. The results are in high agreement with their LSV behavior (Fig. 3(a) and (b)). The decrease in the resistance from CoZn-0.25 to CoZn-2 can be attributed to the simultaneously increased graphitic degree and ECSA (estimated from the electrochemical double layer capacitance of the catalysts; Figs. 4(d) and S26), which facilitates the electron and mass transfer, respectively. Although the graphitic degree enhances gradually from CoZn-2 to CoZn-4, the corresponding resistance shows a rising trend due to the sharp decreased ECSA. It can be concluded that the high graphitic degree with suitable porous nanostructure of ORR catalysts is important to the fast electron transfer and efficient reactant diffusion.

Given the discussions above, the enhancement of ORR by tuning the intrinsic active site and the nanostructure is proposed and illustrated in Fig. 4(e). For the carbon material derived from LDH@ZIF-CoZn-*x* with a high Zn content, despite of an enhanced N doping, a large amount of amorphous carbon with poor conductivity is produced, which lower the catalytic activity toward the dynamic process of ORR. Thus a two-electron transfer pathway with a high HO₂⁻ yield occurs in the oxygen reduction process (Figs. 3(d); 4(e) (I)). In the case of an excess of Co content, although a high graphitization degree with good conductivity is achieved, the concentration of doped-N is drastically reduced due to the higher C–C bonding energy than that of C–N bonding. This thereby decreases the number of active sites for ORR. Besides, an overhigh graphitized carbon would limit the active sites exposure and block the tunnels for ions transport (Figs. 2(c), (d); 4(e), (II)). Therefore, an optimal Co/Zn molar ratio in the Co, Zn-ZIF precursors is crucial to impose a synergistic effect between active sites and surface properties of the derived carbon products, giving rise to the best electrocatalytic performance (Fig. 4(e) (III)).

4. Conclusion

In summary, an effective strategy to artificially regulate the nanostructure and intrinsic active site of carbon-based ORR catalysts has been developed by pyrolysis bimetallic Co, Zn-ZIF crystal arrays grown on the surface of LDHs. By tuning the Co/Zn molar ratio in the Co, Zn-ZIF precursor, the concentration of doped-heteroatoms (N, Co), the graphitic degree and the porous structure of the obtained carbon materials can be finely controlled. The resulting CoZn-2 material shows the highest specific surface area, a relatively high content of N-doping and a suitable graphitization degree, which exhibits remarkable oxygen-reduction activity, extraordinary long-term stability and excellent tolerance against methanol corrosion. It is expected that the obtained 2D carbon-based network in this work can be used as a promising ORR catalyst for efficient energy storage and conversion systems.

Acknowledgments

This work was supported by the National Natural Science Foundation of China (NSFC), the 973 Program (Grant no. 2014CB932102) and the Fundamental Research Funds for the Central Universities (buctrc201506; YS 1406). M. Wei particularly appreciates the financial aid from the China National Funds for Distinguished Young Scientists of the NSFC.

Appendix A. Supplementary material

Supplementary data associated with this article can be found in the online version at <http://dx.doi.org/10.1016/j.nanoen.2016.04.041>.

References

- [1] G. Tian, Q. Zhang, B. Zhang, Y. Jin, J. Huang, D. Su, F. Wei, *Adv. Funct. Mater.* 24 (2014) 5956–5961.
- [2] X. Zhang, X. Lu, Y. Shen, J. Han, L. Yuan, L. Gong, Z. Xu, X. Bai, M. Wei, Y. Tong, Y. Gao, J. Chen, J. Zhou, Z.L. Wang, *Chem. Commun.* 47 (2011) 5804–5806.
- [3] C. Tang, H. Wang, H. Wang, Q. Zhang, G. Tian, J. Nie, F. Wei, *Adv. Mater.* 27 (2015) 4516–4522.
- [4] D. Wang, D. Su, *Energy Environ. Sci.* 7 (2014) 576–591.
- [5] Y. Liang, Y. Li, H. Wang, J. Zhou, J. Wang, T. Regier, H. Dai, *Nat. Mater.* 10 (2011) 780–786.
- [6] J.S. Lee, S.T. Kim, R. Cao, N.S. Choi, M. Liu, K.T. Lee, J. Cho, *Adv. Energy Mater.* 1 (2011) 34–50.
- [7] J. Zhu, M. Xiao, X. Zhao, C. Liu, J. Ge, W. Xing, *Nano Energy* 13 (2015) 318–326.
- [8] X. Sun, D. Li, Y. Ding, W. Zhu, S. Guo, Z.L. Wang, S. Sun, *J. Am. Chem. Soc.* 136 (2014) 5745–5749.
- [9] D. Raciti, J. Kubal, C. Ma, M. Barclay, M. Gonzalez, M. Chi, J. Greeley, K.L. More, C. Wang, *Nano Energy* 20 (2016) 202–211.
- [10] R. Bashyam, P. Zelenay, *Nature* 443 (2006) 63–66.
- [11] G. Wu, P. Zelenay, *Acc. Chem. Res.* 46 (2013) 1878–1889.
- [12] J. Suntivich, H.A. Gasteiger, N. Yabuuchi, H. Nakanishi, J.B. Goodenough, Y. Shao-Horn, *Nat. Chem.* 3 (2011) 546–550.
- [13] R. Cao, J.S. Lee, M. Liu, J. Cho, *Adv. Energy Mater.* 2 (2012) 816–829.
- [14] L. An, H. Yan, X. Chen, B. Li, Z. Xia, D. Xia, *Nano Energy* 20 (2016) 134–143.
- [15] B. Cao, G.M. Veith, R.E. Diaz, J. Liu, E.A. Stach, R.R. Adzic, P.G. Khalifah, *Angew. Chem. Int. Ed.* 52 (2013) 10753–10757.
- [16] J. Liang, X. Du, C. Gibson, X. Du, S. Qiao, *Adv. Mater.* 25 (2013) 6226–6231.
- [17] Y. Li, W. Zhou, H. Wang, L. Xie, Y. Liang, F. Wei, J. Idrobo, S.J. Pennycook, H. Dai, *Nat. Nanotech* 7 (2012) 394–400.
- [18] S. Gao, K. Geng, *Nano Energy* 6 (2014) 44–50.
- [19] L. Shang, H. Yu, X. Huang, T. Bian, R. Shi, Y. Zhao, G.I.N. Waterhouse, L. Wu, C. Tung, T. Zhang, *Adv. Mater.* 28 (2016) 1668–1674.
- [20] Z. Yang, Z. Yao, G. Li, G. Fang, H. Nie, Z. Liu, X. Zhou, X. Chen, S. Huang, *ACS Nano* 6 (2012) 205–211.
- [21] Y. Zhu, B. Zhang, X. Liu, D. Wang, D. Su, *Angew. Chem. Int. Ed.* 53 (2014) 10673–10677.
- [22] S. Gao, L. Li, K. Geng, X. Wei, S. Zhang, *Nano Energy* 16 (2015) 408–418.
- [23] K. Gong, F. Du, Z. Xia, M. Durstock, L.M. Dai, *Science* 323 (2009) 760–764.
- [24] Z. Wu, P. Chen, Q. Wu, L. Yang, Z. Pan, Q. Wang, *Nano Energy* 8 (2014) 118–125.
- [25] W. Xia, R. Zou, L. An, D. Xia, S. Guo, *Energy Environ. Sci.* 8 (2015) 568–576.
- [26] S. Zhao, H. Yin, L. Du, L. He, K. Zhao, L. Chang, G. Yin, H. Zhao, S. Liu, Z. Tang, *ACS Nano*, 8, (2014) 12660–12668.
- [27] S. Ma, G.A. Goenaga, A.V. Call, D. Liu, *Chem. Eur. J.* 17 (2011) 2063–2067.
- [28] K. Chizari, A. Vena, L. Laurentius, U. Sundararaj, *Carbon* 68 (2014) 369–379.
- [29] W. Zhang, Z. Wu, H. Jiang, S. Yu, *J. Am. Chem. Soc.* 136 (2014) 14385–14388.
- [30] Z. Yao, H. Nie, Z. Yang, X. Zhou, Z. Liu, S. Huang, *Chem. Commun.* 48 (2012) 1027–1029.
- [31] Z. Li, M. Shao, L. Zhou, R. Zhang, C. Zhang, M. Wei, D.G. Evans, X. Duan, *Adv. Mater.* 28 (2016) 2337–2344.
- [32] J. Sun, H. Liu, X. Chen, D.G. Evans, W. Yang, X. Duan, *Adv. Mater.* 25 (2013) 1125–1130.
- [33] J. Tang, R.R. Salunkhe, J. Liu, N.L. Torad, M. Imura, S. Furukawa, Y. Yamauchi, *J. Am. Chem. Soc.* 137 (2015) 1572–1580.
- [34] Y. Hou, Z. Wen, S. Cui, S. Ci, S. Mao, J. Chen, *Adv. Funct. Mater.* 25 (2015) 872–882.
- [35] Y. Chen, C. Wang, Z. Wu, Y. Xiong, Q. Xu, S. Yu, H. Jiang, *Adv. Mater.* 27 (2015) 5010–5016.
- [36] X. Wang, J. Zhou, H. Fu, W. Li, X. Fan, G. Xin, J. Zheng, X. Li, *J. Mater. Chem. A* 2 (2014) 14064–14070.
- [37] H. Zhong, J. Wang, Y. Zhang, W. Xu, W. Xing, D. Xu, Y. Zhang, X. Zhang, *Angew. Chem. Int. Ed.* 53 (2014) 14235–14239.
- [38] Z. Yuan, T. Ren, A. Vantomme, B. Su, *Chem. Mater.* 16 (2004) 5096–5106.
- [39] W. Xia, A. Mahmood, Z. Liang, R. Zou, S. Guo, *Angew. Chem. Int. Ed.* 55 (2016) 2650–2676.
- [40] W. Xia, A. Mahmood, R. Zou, Q. Xu, *Energy Environ. Sci.* 8 (2015) 1837–1866.
- [41] J. Liang, Y. Zheng, J. Chen, J. Liu, D. Hulicova-Jurcakova, M. Jaroniec, S. Qiao, *Angew. Chem. Int. Ed.* 51 (2012) 3892–3896.
- [42] M. Shao, F. Ning, Y. Zhao, J. Zhao, M. Wei, D.G. Evans, X. Duan, *Chem. Mater.* 24 (2012) 1192–1197.
- [43] X. Xia, J. Tu, Y. Zhang, X. Wang, C. Gu, X. Zhao, H. Fan, *ACS Nano* 6 (2012) 5531–5538.



Mingfei Shao received his PhD degree from Beijing University of Chemical Technology in 2014, after which he joined the staff of BUCT. He was also a visiting student at the University of Oxford in 2013. His current research interests are mainly focused on the controlled synthesis of layered functional materials and their applications in electrochemical and photoelectrochemical energy storage and conversions.



Lei Zhou received her Bachelor's degree in 2013 from Beijing University of Chemical Technology. She joined Prof. Xue Duan's group as a PhD candidate at Beijing University of Chemical Technology in 2013. Her research interests currently focus on the design and fabrication of electrodes for small molecules electrocatalysis.



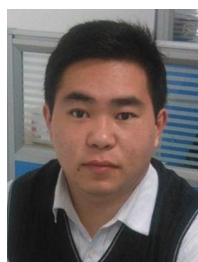
Qihui Yang received her Bachelor's degree in 2015 from Henan University of Technology. She is now a post-graduate under the supervision of Dr. Mingfei Shao in Beijing University of Chemical Technology (BUCT). Her research interests currently focus on the fabrication of electrode materials for energy storage.



Cong Zhang received her Bachelor's degree in 2012 from Yanching Institute of Technology. She is now a PhD candidate under the supervision of Prof. Min Wei in the Beijing University of Chemical Technology (BUCT). Her research interests mainly focus on the design and fabrication of oxygen evolution reaction (OER) catalysts for electrochemical water splitting.



Min Wei obtained her BEng degree in 1995 and MEng degree in 1998 from Beijing University of Chemical Technology (BUCT). She subsequently received her PhD from Peking University in 2001, after which she joined the staff of BUCT. She was promoted to full Professor in 2005. She has been a visiting scholar in the Georgia Institute of Technology (in 2008). Her research interests focus on inorganic-organic composite functional materials as well as new catalysts.



Zhenhua Li received his Bachelor's degree from Beijing University of Chemical Technology (BUCT) in Polymer Science and engineering in 2014. He is now a PhD candidate under the supervision of Prof. Xue Duan in the BUCT. His research interests mainly focus on the synthesis of nanostructured layered double hydroxides and their application in the energy storage and conversion.



David G. Evans studied as both an undergraduate and a research student at Jesus College, Oxford, and obtained a DPhil under the supervision of Prof. D. M. P. Mingos FRS. After postdoctoral work at Bristol University with Prof. F. G. A. Stone FRS, he was appointed as a lecturer at Exeter University in 1985. Several visits to Chinese university chemistry departments in the early 1990s convinced him of China's great potential for development and he moved to Beijing University of Chemical Technology in 1996. His research interests focus on intercalation in layered solids.



Xue Duan was elected as an Academician of the Chinese Academy of Sciences in 2007. He was awarded his BS degree from Jilin University and MS and PhD degrees from Beijing University of Chemical Technology (BUCT). He was subsequently appointed to the staff of BUCT and established the Applied Chemistry Research Institute in 1990. He was promoted to full Professor in 1993 and to PhD supervisor status in 1995. He is currently Director of the Institute of Applied Chemistry and Executive Vice-Chair of the Academic Committee of the State Key Laboratory of Chemical Resource Engineering.